Superconducting phase diagram of finite-layer nickelates $\mathbf{Nd}_{n+1}\mathbf{Ni}_n\mathbf{O}_{2n+2}$

Andreas Hausoel ⓘ,[1, *] Simone Di Cataldo ⓘ,[2, *] Motoharu Kitatani ⓘ,[3] Oleg Janson ⓘ,[1] and Karsten Held ⓘ[4]

[1]*Institute for Theoretical Solid State Physics, Leibniz Institute for Solid State*
and Materials Research Dresden, Helmholtzstr. 20, 01069 Dresden, Germany
[2]*Dipartimento di Fisica, Sapienza Università di Roma, Piazzale Aldo Moro 5, 00187 Roma, Italy*
[3]*Department of Material Science, University of Hyogo, Ako, Hyogo 678-1297, Japan*
[4]*Institute of Solid State Physics, TU Wien, 1040 Vienna, Austria*
(Dated: February 18, 2025)

Following the successful prediction of the superconducting phase diagram for infinite-layer nicke-lates, here we calculate the superconducting T_c vs. the number of layers n for finite-layer nickelates using the dynamical vertex approximation. To this end, we start with density functional theory, and include local correlations non-perturbatively by dynamical mean-field theory for $n = 2$ to 7. For all n, the Ni $d_{x^2-y^2}$ orbital crosses the Fermi level, but for $n > 4$ there are additional (π, π) pockets or tubes that slightly enhance the layer-averaged hole doping of the $d_{x^2-y^2}$ orbitals beyond the leading $1/n$ contribution stemming from the valence electron count. We finally calculate T_c for the single-orbital $d_{x^2-y^2}$ Hubbard model by dynamical vertex approximation.

I. INTRODUCTION

The discovery of superconductivity in nickelates by Li, Hwang *et al.* [1] has opened a new and very active area of research. In fact, superconducting nickelates remain a largely unexplored family of strongly-correlated systems, and offer researchers a unique and novel testbed to study unconventional superconductivity.

However, synthesizing infinite-layer nickelates $(Ca,Sr)_x R_{1-x}NiO_2$ with rare earth R = Nd, La, Pr, Sm that are actually superconducting has proved to be challenging, and only a few groups succeeded [2–14]. The primary obstacle to synthesize superconducting nickelate films and bulk materials is the large degree of disorder, stacking faults and off-stoichiometry. This is caused by the complicated synthesis process which involves first growing $(Ca,Sr)_x R_{1-x}NiO_3$ and then reducing it to $(Ca,Sr)_x R_{1-x}NiO_2$ with CaH_2 or H [13, 15]. The necessity to hole-dope the system into the superconducting state with Ca (or Sr) increases the chances of disorder. This, in combination with the oxygen reduction, prevents synthesizing bulk nickelates with $x > 8\%$ [16]. It is not surprising that, even among the superconducting films, there is a large variance in the measured properties. Cleaner films show resistivities lower by a factor of three, while at the same time, the critical temperature T_c is considerably larger [9, 10].

Against this background, growing finite-layer nickelate films $Nd_{n+1}Ni_nO_{2n+2}$, see Fig. 1 (top), offers a welcome alternative to doping infinite-layer nickelates with Sr or Ca, eliminating at least Sr/Ca disorder. This second family of nickelates presents a series of finite slabs separated by a stacking fault (black dashed lines in Fig. 1) that is delineated by an additional O layer and a shift by half-of-the-unit-cell diagonal perpendicular to the stacking fault. These finite-layer nickelates are a generaliza-
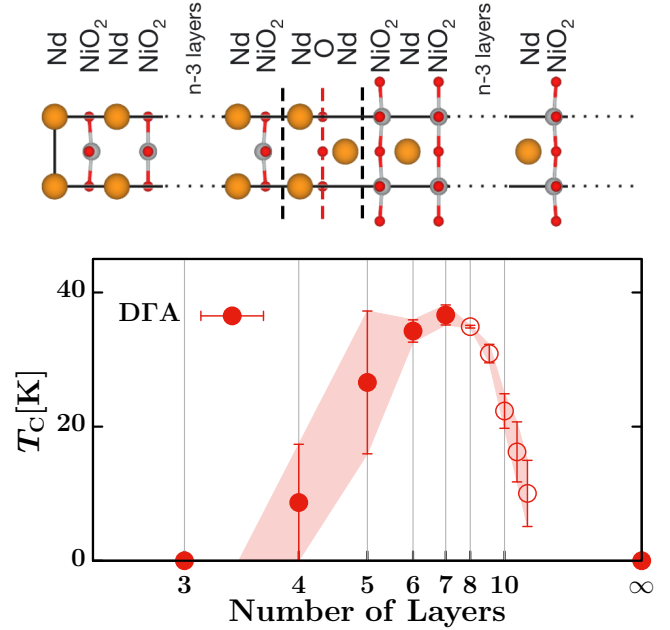

FIG. 1. **Top: Crystal structure** of finite-layer nicke-lates $Nd_{n+1}Ni_nO_{2n+2}$. Nd, Ni, and O atoms are indicated as large orange, medium grey, and small red spheres, respectively. Dashed black lines indicate the Nd–O–Nd stacking fault. **Bottom: Phase diagram.** superconducting T_c vs. number of layers n as calculated by DΓA. The error bar reflects the uncertainty in the hole doping of the $d_{x^2-y^2}$ orbital, as discussed in Section II C; the open circle for $n \geq 8$ indicates that we here used an infinite-layer calculation with total doping $1/n$ to mimic the finite layer nickelate.

tion of infinite-layer ones that are recovered for $n \to \infty$. These finite-layer nickelates are not to be confused with the Ruddlesden-Popper series $La_{n+1}Ni_nO_{3n+1}$ [17] whose Ni $3d$ shells are filled with $(7 + \frac{1}{n})$ electrons, i.e. between 7 and 8, instead of $(9 - \frac{1}{n})$ for the finite-layer nickelates considered here.

* These authors contributed equally.

Pan, Mundy *et al.* established the presence of superconductivity in finite-layer nickelates for $n = 5$ [6] and reported ongoing work for other n [18]. Similar layered compounds can also form with copper, such as $Tl_2Ba_2Ca_{n-1}Cu_nO_{2n+4}$ [19] and $HgBa_2Ca_{n-1}Cu_nO_{2n+2}$ [20], in which the T_c is typically maximal for $n = 3$. In a fashion similar to cuprates, it is likely that finite-layer nickelates are far from having reached the optimum T_c, as both the number of layers and sample quality can still be optimized.

Moving on to the theoretical studies, superconductivity in bulk nickelates [21] and nickelate heterostructures [22] has been conjectured long before samples were successfully synthesized. Only after their synthesis in 2019 [1], however, were they thoroughly examined on the theoretical side, turning them into the *hot* topic they currently are [23–33].

The arguably simplest description for $3d^9$ nickelates is that of a one-band Hubbard model plus largely detached pockets originating from the Nd $5d$ orbitals [34, 35]. This simple description was recently confirmed by angular-resolved photoemission spectroscopy (ARPES) that only showed a Ni $3d_{x^2-y^2}$ Fermi surface and a pocket at (π, π, π) ("A pocket") for $Sr_xLa_{1-x}NiO_2$ [36, 37], in excellent agreement with *a priori* density functional theory (DFT) plus dynamical mean-field theory (DMFT) calculations [34, 38]. Even the superconducting dome determined with the dynamical vertex approximation (DΓA) [34] well agrees with *a posteriori* experiments [9], as does the resonant inelastic X-ray spectrum [39, 40]. Finite-layer nickelates have been also studied theoretically [41, 42], though hitherto with a focus on the pentalayer found in the first experiment [6].

In this letter we calculated the T_c vs. number of layers n phase diagram for finite-layer neodymium nickelates on a neodymium gallium oxide substrate. We employed DFT to determine the crystal structure of such strained superlattices and calculate their electronic structure. From there, we included local correlations using DMFT in Ni $3d$ and Nd $5d$ shells, and finally mapped the result to the minimal single-band model to estimate the superconducting T_c by DΓA. This brings us to the central result of our work – the phase diagram in Fig. 1, showing the dome-like behavior of the superconducting T_c vs. an increasing (from left to right) number of layers n. Superconductivity is found for a similar number of layers as in experiment ($n = 4 - 8$ [18]).

II. RESULTS

A. Density functional theory

The crystal structures for the $Nd_{n+1}Ni_nO_{2n+2}$ series were constructed starting from a supercell of n infinite-layer unit cells and adding the stacking fault. The in-plane lattice parameters were constrained to those of cubic $NdGaO_3$ (NGO), i.e. $a = b = 3.83$Å, which experi-
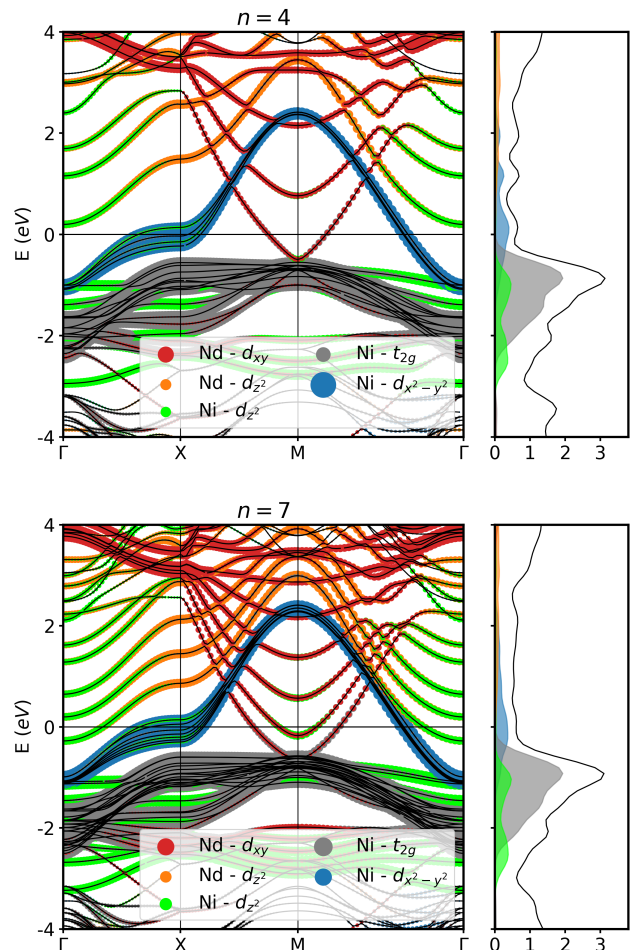

FIG. 2. **DFT band structure and DOS** atom- and orbital-projected for $n = 4$ and $n = 7$; see Supplemental Note SVII [43] for $n = 2, 3, 5, 6$ and ∞. The bands are colored with the projection onto the atomic orbitals. Red, grey, orange, blue, and green indicate Nd d_{xy}, Ni t_{2g}, Nd d_{z^2}, Ni $d_{x^2-y^2}$, and Ni d_{z^2} orbitals, respectively. The DOS is indicated in units of states/eV/Ni; projections onto atomic orbitals follow the same color coding as the bands.

mentally is used as a substrate [6, 18], while the c axis was relaxed as in Ref. [44], see Supplementary Note SV.

There is an out-of-plane distortion of the Ni-O bonds, clearly visible in the true-to-scale Fig. 1 (top), which is particularly strong for the layers facing the stacking fault ($4°$), and rapidly fades in further layers. See Supplemental Note SV for details on the distortion angles and further information on the DFT relaxation; and Section IV for the methods and codes used. The interaction with the stacking fault causes a substantial difference between *outer* (close to the stacking fault) and *inner* (away from the stacking fault) Ni-O layers. This interaction also introduces a symmetry inequivalence between odd-n and even-n cases, for which $n = 2$ represents a further special case in which only outer layers are present.

In Fig. 2 we report the DFT-calculated band structure

and density of states (DOS), projected onto the most relevant atomic orbitals for $n = 4$ and $n = 7$ layers (for the other values of n we refer the reader to the Supplemental Note SVII [43]). For both n's, bands of Ni $d_{x^2-y^2}$ and Nd d_{xy} character cross the Fermi energy. The latter forms the A pocket of the infinite-layer nickelate which becomes one or several M–A tubes for the finite-layer compound, see Supplementary Note SVII [43]. Without the stacking fault, we would have just the infinite-layer structure, but with a backfolding of n k_z's into n vineyard-like bands for a supercell of n layers. We see this general pattern, but the stacking fault also leads to marked differences, particularly for small n. Most noteworthy, the stacking faults lift the Γ pocket which has Nd and Ni d_{z^2} character and is still present for $n = 7$ above the Fermi energy for $n = 4$. The projected DOS in Fig. 2 (left) also shows predominantly Ni $d_{x^2-y^2}$ character at the Fermi level, with Ni t_{2g} and d_{z^2} bands further below and Nd bands above. Changes of the DOS are quite minute when changing the number of layers n.

B. Dynamical mean-field theory

Due to the partially occupied $3d$ states, specifically the roughly half-filled Ni $3d_{x^2-y^2}$ orbital, electronic correlations beyond DFT are important and we take these into account, on a first level, by DMFT [45, 46]. To this end, we perform Wannier projections of the band structure onto a model of Ni $3d$ and Nd $5d$ states. Next, we supplement the Wannier-projected Hamiltonian by a local intra-orbital Coulomb interaction of $U = 4.4$ eV (2.5 eV) and a Hund's exchange $J = 0.65$ eV (0.25 eV) for the five Ni(Nd) $3d$ orbitals, as calculated previously in constrained random phase approximation (cRPA) [33, 34] and used throughout our work [34, 40, 41, 44]. For details of the Wannier projection and the hopping parameters, see the Supplemental Note SVI [43].

Constructing accurate Wannier projections for large-n superlattices becomes very cumbersome. Yet, such models are also dispensable, because in this limit the physics of finite-layer nickelates hardly differs from infinite-layer NdNiO$_2$. Hence, for $n \geq 8$, we restrict ourselves to five–plus–five DMFT infinite-layer calculations for one formula unit and a total filling of $(9 - 1/n)$ of all ten orbitals. These "infinite-layer" results are indicated in Fig. 1 (above) and Fig. 4 (below) through open circles and continue those of the actual finite-layer calculations quite smoothly with only a minor kink.

Fig. 3 shows the DMFT **k**-resolved and **k**-integrated spectral function, $A(\mathbf{k}, \omega)$ and $A(\omega)$, that can be directly compared, respectively, with the DFT-calculated band structure and DOS. We see an upshift of the Γ pocket above the Fermi energy also for $n = 7$ in DMFT. For $n = 4$ now also the A pocket is shifted above the Fermi level, while it still crosses the Fermi energy for $n = 7$. Only the Ni $d_{x^2-y^2}$ orbital that crosses the Fermi level has a strong quasiparticle renormalization $Z = 0.32$ for $n = 4$
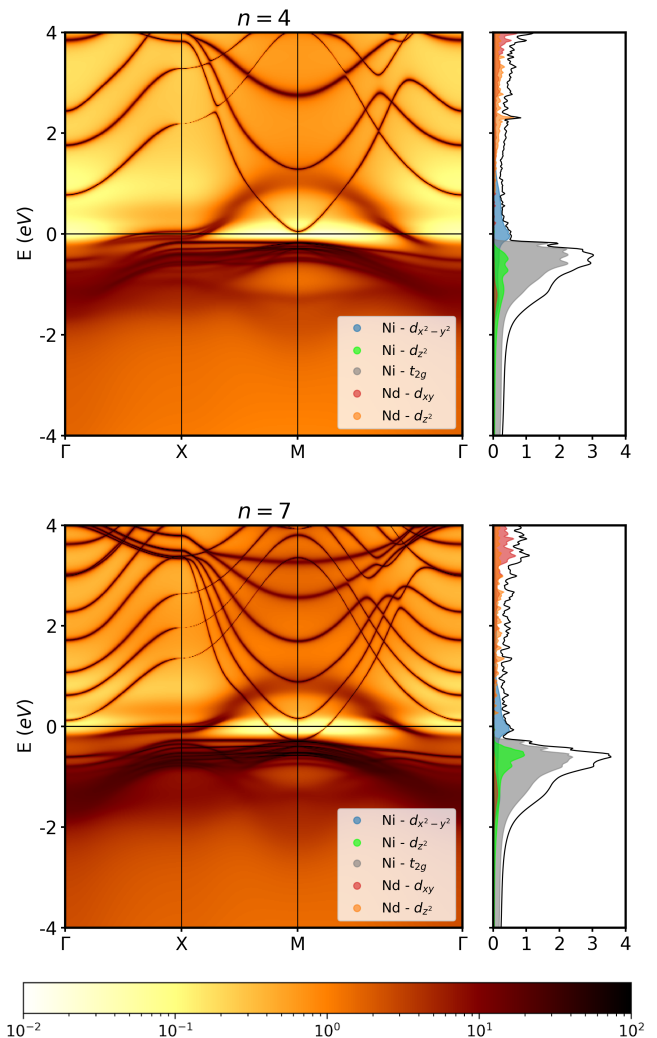

FIG. 3. **DMFT electronic structure (left) and DOS (right)** of Nd$_{n+1}$Ni$_n$O$_{2n+2}$ for $n = 4$ (top) and $n = 7$ layers (bottom) and room temperature; see Supplemental Note SVIII [43] for $n = 2, 3, 5, 6, \infty$.

and $Z = 0.26$ for $n = 7$, which also causes a finite-lifetime broadening compared to the bare DFT dispersion. The renormalizations Z of all other orbitals remain close to one, see Supplemental Note SVIII [43]. Further we see some broadened lower Hubbard band around -0.8 eV which comprises all Ni d orbitals.

For determining the proper number of electrons in the Ni $d_{x^2-y^2}$ orbital, the filling of the A pocket needs to be taken into account. In the Supplemental Note SIX [43], we determine the DMFT hole doping due to the A pocket to be roughly $\delta_{\text{pocket}} \approx 0.02 - 0.08 \times 1/n$ for $n > 4$ and zero for $n \leq 4$ where there is no A pocket.

Fig. 4 compares the filling of the Ni $d_{x^2-y^2}$ orbital with this hole doping $(1 - 1/n - \delta_{\text{pocket}})/2$ to the DMFT occupation of the $d_{x^2-y^2}$ orbital, where the factor $1/2$ account for the spin. For larger n both well agree, though the infinite-layer compound somewhat deviates from our
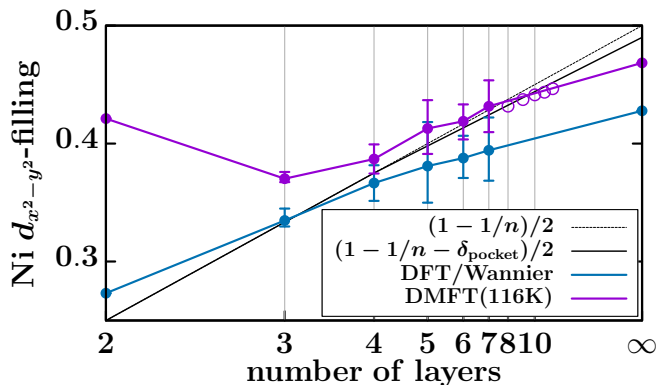
FIG. 4. **Average Ni $d_{x^2-y^2}$ occupation as a function of the number of layers** n comparing DMFT at $100\,\mathrm{K}$ (which is almost identical to $300\,\mathrm{K}$) and DFT to the formal valence count with and without including the self-doping through the A pocket.

δ_{pocket} fitted to finite-layer nickelates. For $n \lesssim 4$, on the other hand, we see deviations in DMFT. The reason for these deviations is two-fold: (i) There is some, actually quite small admixture of the Ni $d_{x^2-y^2}$ orbital with the other Ni and Nd orbitals. Both give opposite effects for the filling of Ni $d_{x^2-y^2}$ orbital and essentially cancel for $n > 4$. When the number of layers is smaller this is not the case any more because the Nd layers adjacent to the stacking faults do not contribute in this admixture, see Supplemental Note SVIII [43] for a detailed discussion. (ii) For $n = 2$, the Ni d_{z^2} orbital crosses the Fermi level in DMFT (but not in DFT; see Supplemental Note SVIII [43]). Its depopulation allows the Ni $d_{x^2-y^2}$ orbital to stay closer to half-filling.

Fig. 5 further shows the layer- and orbital-resolved DMFT occupation for $n = 7$, with the aforementioned orbital admixture leading to a Ni d_{z^2} occupation around 0.9 instead of 1, some Nd d_{z^2} occupation and a Nd d_{xy} occupation larger than what to expect from the size of the A pocket alone. Most importantly however, for the Ni $d_{x^2-y^2}$ orbital we observe a quite strong layer dependence. There are sizably more holes in the layers adjacent to the extra O at the stacking fault (red layer) that is responsible for the hole doping in the first place.

C. Dynamical vertex approximation

By construction, DMFT accounts only for local correlations. To include non-local correlations and calculate the superconducting T_c, the Hamiltonian with $n \times 5$ Ni $3d$ and $(n+1) \times 5$ Nd $5d$ orbitals is way beyond the current technical limitations. However, the DMFT clearly shows the prevalence of the Ni $3d_{x^2-y^2}$ orbital; and the Nd-derived band(s) crossing the Fermi level around A (and M), do not hybridize in the bulk with the Ni $3d_{x^2-y^2}$ orbital. Also for the finite-layer nickelates this hybridization is weak. Hence, we describe the superconducting
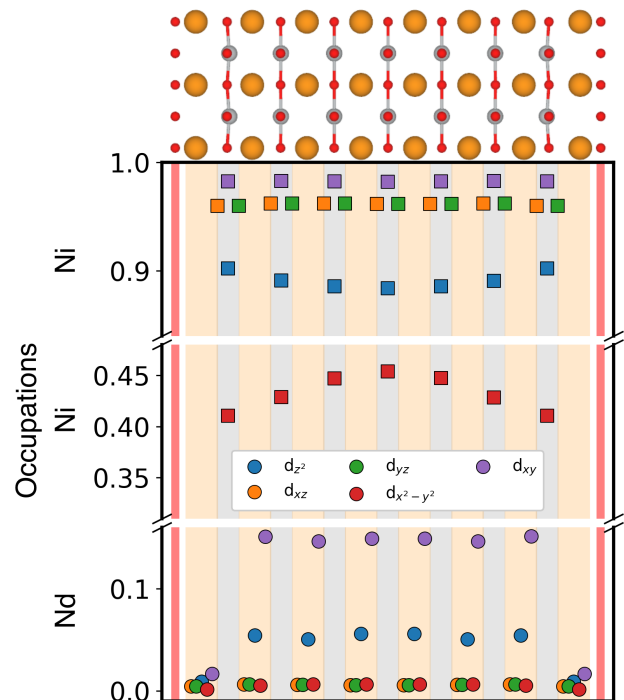

FIG. 5. **Orbital occupations for each Ni and Nd atom of $Nd_8Ni_7O_{16}$ ($n = 7$) as calculated by DMFT**; see Supplemental Note SVIII [43] for other n. The top of the figure shows the crystal structure with Nd, Ni and O atoms displayed in orange, grey, and red, respectively. The same color code is used in the bottom part for the background stripes to visualize the Nd, Ni(O$_2$), and stacking-fault O planes. Orbital occupations of Ni and Nd are displayed in their respective stripe and represented as squares and circles, respectively, with the color code for the different $3d$ respectively $5d$ orbitals given in the legend box. Note the broken y-axis with the almost empty Nd, half-filled Ni $d_{x^2-y^2}$, and nearly occupied other Ni orbitals.

properties of the compound as in infinite-layer nickelates [34], i.e. we restrict ourselves to a single $3d_{x^2-y^2}$ orbital per NiO$_2$ layer and do an additional Wannier projection onto this single orbital. The hopping parameters of this one-Ni-$d_{x^2-y^2}$-orbital model are given in the Supplemental Information SVI; and the Hubbard interaction U for this single orbital must be somewhat smaller due to additional screening. We use the same cRPA-estimated $U = 8t$ as in Ref. [34].

Given the rather weak inter-layer hopping t_z, we then solve a two-dimensional Hubbard model with DΓA [34, 47–49]. We find d-wave superconductivity induced by antiferromagnetic spin fluctuations and the phase diagram has been already presented in Fig. 1. As different layers exhibit slightly different hoppings and dopings, see Fig. 4, we give – as a fair estimate of the error bar – the minimal and maximal T_c for three dopings: average DMFT $d_{x^2-y^2}$ occupation; layer with optimal DMFT $d_{x^2-y^2}$ occupation; and $(1-1/n-\delta_{\mathrm{pocket}})/2$. The in-plane hopping parameters are quite constant for all n and all

layers, see Supplementary Note SVI, and well described by $t=420$ meV, $t' = -0.25t$, $t'' = 0.12t$.

III.   DISCUSSION

Using state-of-the-art DFT, DMFT, and DΓA we have calculated the superconducting phase diagram of finite-layer nickelates $Nd_{n+1}Ni_nO_{2n+2}$ on a $NdGaO_3$ substrate. In agreement with preliminary experimental results [18], we obtain superconductivity for $n \approx 4-9$ layers, where we have mimicked $n \geq 8$ by a hole-doped infinite-layer Wannier Hamiltonian. Compared to the first infinite-layer experiments, [6, 18] the calculated T_c values are somewhat higher. However, the timeline of reported T_c in infinite-layer nickelates makes us hopeful that further experiments and improved synthesis will enhance T_c also in finite-layer nickelates.

Only the Ni $d_{x^2-y^2}$ orbital and the A pocket cross the Fermi energy. A somewhat unexpected result is that the hopping parameters for the Ni $d_{x^2-y^2}$ orbital do *not* depend on the layer index nor on the number of layers n. This is a consequence of growing the nickelates on a $NdGaO_3$ substrate, thus fixing the in-plane lattice constant; and the tilting at the stacking fault is, in hindsight, not large enough for changing the hopping parameters substantially. This practical universality of the hopping parameters is very different from the cuprates that are synthesized as bulk materials and are thus much more versatile in their in-plane lattice constant.

However, there is quite a strong layer dependence of the Ni $d_{x^2-y^2}$ orbital occupation. This is relevant for the superconducting T_c. Within the constraints of what is presently feasible, we take this layer-dependent doping into account by calculating T_c in DΓA for a two-dimensional single-$d_{x^2-y^2}$-orbital Hubbard model, with the error bars in Fig. 1 reflecting in particular the uncertainties and layer-dependencies of the doping of the Ni $d_{x^2-y^2}$ orbital. This uncertainty results in a particular large error bar for $n = 4$. We feel that, nonetheless and with this caveat in mind, our calculation of the phase diagram is accurate and reliable, without any adjusted parameters.

IV.   METHODS

In this section, we summarize the computational methods employed. The interested reader can find additional information in [44] (including its Supplemental Information) and [34, 50]; data and input files for the whole set of calculations in the associated data repository XXX.

Density functional theory calculations were performed using the Vienna ab-initio simulation package (VASP) [51, 52] using projector-augmented wave pseudopotentials and Perdew-Burke-Ernzerhof exchange correlation functional adapted for solids (PBESol) [53, 54], with a cutoff of 1000 eV for the plane wave expansion. Integration over the Brillouin zone was performed over a grid with a uniform spacing of $0.25\,Å^{-1}$ and a Gaussian smearing of 0.20 eV. Wannierization was performed using `wannier90` [55].

The crystal structures structures were relaxed first by fixing the in-plane lattice parameter to the $NdGaO_3$ value (reference substrate, 3.83 Å). Then the internal coordinates were relaxed along with the c axis as in Ref. [44].

DMFT calculations were performed using `w2dynamics` [56], with values of U and J as detailed in the main text at room temperature (300 K) and 100 K.

For obtaining T_c, we employed the ladder DΓA with the λ correction as done before in Refs. [34, 57–59]. To evaluate T_c of the target fillings for drawing the phase diagram, we interpolated (extrapolated) the DΓA results for Ni $d_{x^2-y^2}$ fillings $n = 0.775, 0.80, 0.825, 0.85, 0.875, 0.90$, which were obtained from Ref. [34].

AUTHOR CONTRIBUTIONS

S.D.C. performed the DFT calculations and wannierization, A.H. the DMFT calcualtions, M.K. calculated the DΓA T_c. O.J. and K.H. devised and supervised the project, and K.H. did the major part of the writing. All authors discussed and refined the project, contributed to the writing and and approved the submitted version.

COMPETING INTERESTS

The authors declare that they have no competing interests.

DATA AND MATERIALS AVAILABILITY

The raw data for the figures reported, along with input and output files is available at XXX.

[1] D. Li, K. Lee, B. Y. Wang, M. Osada, S. Crossley, H. R. Lee, Y. Cui, Y. Hikita, and H. Y. Hwang, Superconductivity in an infinite-layer nickelate, Nature **572**, 624 (2019).

[2] D. Li, B. Y. Wang, K. Lee, S. P. Harvey, M. Osada, B. H. Goodge, L. F. Kourkoutis, and H. Y. Hwang, Superconducting dome in $Nd_{1-x}Sr_xNiO_2$ infinite layer films, Phys. Rev. Lett. **125**, 027001 (2020).

[3] S. Zeng, C. S. Tang, X. Yin, C. Li, M. Li, Z. Huang, J. Hu, W. Liu, G. J. Omar, H. Jani, Z. S. Lim, K. Han, D. Wan, P. Yang, S. J. Pennycook, A. T. S. Wee, and A. Ariando, Phase diagram and superconducting dome of infinite-layer $Nd_{1-x}Sr_xNiO_2$ thin films, Phys. Rev. Lett. **125**, 147003 (2020).

[4] M. Osada, B. Y. Wang, K. Lee, D. Li, and H. Y. Hwang, Phase diagram of infinite layer praseodymium nickelate $Pr_{1-x}Sr_xNiO_2$ thin films, Phys. Rev. Mater. **4**, 121801 (2020).

[5] S. Zeng, C. Li, L. E. Chow, Y. Cao, Z. Zhang, C. S. Tang, X. Yin, Z. S. Lim, J. Hu, P. Yang, and A. Ariando, Superconductivity in infinite-layer nickelate $La_{1-x}Ca_xNiO_2$ thin films, Sci. Adv. **8**, eabl9927 (2022).

[6] G. A. Pan, D. F. Segedin, H. LaBollita, Q. Song, E. M. Nica, B. H. Goodge, A. T. Pierce, S. Doyle, S. Novakov, D. C. Carrizales, A. T. N'Diaye, P. Shafer, H. Paik, J. T. Heron, J. A. Mason, A. Yacoby, L. F. Kourkoutis, O. Erten, C. M. Brooks, A. S. Botana, and J. A. Mundy, Superconductivity in a quintuple-layer square-planar nickelate, Nat. Mater. **21**, 160 (2021).

[7] M. Osada, B. Y. Wang, B. H. Goodge, S. P. Harvey, K. Lee, D. Li, L. F. Kourkoutis, and H. Y. Hwang, Nickelate superconductivity without rare-earth magnetism: $(La, Sr)NiO_2$, Adv. Mater. **33**, 2104083 (2021).

[8] N. N. Wang, M. W. Yang, Z. Yang, K. Y. Chen, H. Zhang, Q. H. Zhang, Z. H. Zhu, Y. Uwatoko, L. Gu, X. L. Dong, J. P. Sun, K. J. Jin, and J.-G. Cheng, Pressure-induced monotonic enhancement of tc to over 30 K in superconducting $Pr_{0.82}Sr_{0.18}NiO_2$ thin films, Nat. Commun. **13**, 4367 (2022).

[9] K. Lee, B. Y. Wang, M. Osada, B. H. Goodge, T. C. Wang, Y. Lee, S. Harvey, W. J. Kim, Y. Yu, C. Murthy, S. Raghu, L. F. Kourkoutis, and H. Y. Hwang, Linear-in-temperature resistivity for optimally superconducting $(Nd, Sr)NiO_2$, Nature **619**, 288 (2023).

[10] S. L. E. Chow, Z. Luo, and A. Ariando, High-temperature superconducting oxide without copper at ambient pressure, arXiv:2410.00144.

[11] H. Sahib, F. Rosa, A. Raji, G. Merzoni, G. Ghiringhelli, M. Salluzzo, A. Gloter, N. Viart, and D. Preziosi, Superconductivity in $PrNiO_2$ infinite-layer nickelates, arXiv:2410.16147.

[12] W. Xiao, Z. Yang, S. Hu, Y. He, X. Gao, J. Liu, Z. Deng, Y. Hong, L. Wei, L. Wang, *et al.*, Superconductivity in an infinite-layer nickelate superlattice, Nat. Commun. **15**, 10215 (2024).

[13] Y. Lee, X. Wei, Y. Yu, L. Bhatt, K. Lee, B. H. Goodge, S. P. Harvey, B. Y. Wang, D. A. Muller, L. F. Kourk-outis, W.-S. Lee, S. Raghu, and H. Y. Hwang, Synthesis of superconducting freestanding infinite-layer nickelate heterostructures on the millimetre scale, Nat. Synth. 10.1038/s44160-024-00714-2 (2025).

[14] Z. Dong, M. Hadjimichael, B. Mundet, J. Choi, C. C. Tam, M. Garcia-Fernandez, S. Agrestini, C. Domínguez, R. Bhatta, Y. Yu, Y. Liang, Z. Wu, J.-M. Triscone, C. Jia, K.-J. Zhou, and D. Li, Topochemical synthesis and electronic structure of high-crystallinity infinite-layer nickelates on an orthorhombic substrate, Nano Lett. **25**, 1233 (2025).

[15] K. Lee, B. H. Goodge, D. Li, M. Osada, B. Y. Wang, Y. Cui, L. F. Kourkoutis, and H. Y. Hwang, Aspects of the synthesis of thin film superconducting infinite-layer nickelates, APL Materials **8**, 41107 (2020).

[16] P. Puphal, V. Sundaramurthy, V. Zimmermann, K. Küster, U. Starke, M. Isobe, B. Keimer, and M. Hepting, Phase formation in hole- and electron-doped rare-earth nickelate single crystals, APL Materials **11**, 081107 (2023).

[17] H. Sun, M. Huo, X. Hu, J. Li, Z. Liu, Y. Han, L. Tang, Z. Mao, P. Yang, B. Wang, J. Cheng, D.-X. Yao, G.-M. Zhang, and M. Wang, Signatures of superconductivity near 80 K in a nickelate under high pressure, Nature **621**, 493 (2023).

[18] G. A. Pan, D. F. Segedin, S. F. TenHuisen, H. LaBollita, A. Y. Jiang, A. B. Turkiewicz, C. Klewe, C. M. Brooks, I. E. Baggari, A. S. Botana, M. Mitrano, and J. A. Mundy, Correlated phase diagram tunable by structural layering in square-planar nickelates, APS March Meeting 2024 (unpublished).

[19] Z. Z. Sheng and A. M. Hermann, Bulk superconductivity at 120 K in the Tl–Ca/Ba–Cu–O system, Nature **332**, 138 (1988).

[20] A. Schilling, M. Cantoni, J. D. Guo, and H. R. Ott, Superconductivity above 130 K in the Hg–Ba–Ca–Cu–O system, Nature **363**, 56 (1993).

[21] V. I. Anisimov, A. I. Poteryaev, M. A. Korotin, A. O. Anokhin, and G. Kotliar, First-principles calculations of the electronic structure and spectra of strongly correlated systems: Dynamical mean-field theory, J. Phys.: Condens. Matter **9**, 7359 (1997).

[22] P. Hansmann, X. Yang, A. Toschi, G. Khaliullin, O. K. Andersen, and K. Held, Turning a nickelate Fermi surface into a cupratelike one through heterostructuring, Phys. Rev. Lett. **103**, 016401 (2009).

[23] A. S. Botana and M. R. Norman, Similarities and differences between $LaNiO_2$ and $CaCuO_2$ and implications for superconductivity, Phys. Rev. X **10**, 11024 (2020).

[24] H. Sakakibara, H. Usui, K. Suzuki, T. Kotani, H. Aoki, and K. Kuroki, Model Construction and a Possibility of Cupratelike Pairing in a New d^9 Nickelate Superconductor $(Nd, Sr)NiO_2$, Phys. Rev. Lett. **125**, 077003 (2020).

[25] P. Jiang, L. Si, Z. Liao, and Z. Zhong, Electronic structure of rare-earth infinite-layer $RNiO_2$ (R = La, Nd), Phys. Rev. B **100**, 201106 (2019).

[26] M. Hirayama, T. Tadano, Y. Nomura, and R. Arita, Ma-

terials design of dynamically stable d^9 layered nickelates, Phys. Rev. B **101**, 75107 (2020).

[27] X. Wu, D. Di Sante, T. Schwemmer, W. Hanke, H. Y. Hwang, S. Raghu, and R. Thomale, Robust $d_{x^2-y^2}$-wave superconductivity of infinite-layer nickelates, Phys. Rev. B **101**, 60504 (2020).

[28] Y. Nomura, M. Hirayama, T. Tadano, Y. Yoshimoto, K. Nakamura, and R. Arita, Formation of a two-dimensional single-component correlated electron system and band engineering in the nickelate superconductor NdNiO$_2$, Phys. Rev. B **100**, 205138 (2019).

[29] G.-M. Zhang, Y.-F. Yang, and F.-C. Zhang, Self-doped Mott insulator for parent compounds of nickelate superconductors, Phys. Rev. B **101**, 20501 (2020).

[30] M. Jiang, M. Berciu, and G. A. Sawatzky, Critical nature of the Ni spin state in doped NdNiO$_2$, Phys. Rev. Lett. **124**, 207004 (2020).

[31] P. Werner and S. Hoshino, Nickelate superconductors: Multiorbital nature and spin freezing, Phys. Rev. B **101**, 41104 (2020).

[32] J. Karp, A. S. Botana, M. R. Norman, H. Park, M. Zingl, and A. Millis, Many-Body Electronic Structure of NdNiO$_2$ and CaCuO$_2$, Phys. Rev. X **10**, 21061 (2020).

[33] L. Si, W. Xiao, J. Kaufmann, J. M. Tomczak, Y. Lu, Z. Zhong, and K. Held, Topotactic hydrogen in nickelate superconductors and akin infinite-layer oxides ABO$_2$, Phys. Rev. Lett. **124**, 166402 (2020).

[34] M. Kitatani, L. Si, O. Janson, R. Arita, Z. Zhong, and K. Held, Nickelate superconductors – a renaissance of the one-band Hubbard model, npj Quantum Materials **5**, 59 (2020).

[35] K. Held, L. Si, P. Worm, O. Janson, R. Arita, Z. Zhong, J. M. Tomczak, and M. Kitatani, Phase Diagram of Nickelate Superconductors Calculated by Dynamical Vertex Approximation, Front. Phys. (Lausanne) **9**, 810394 (2022).

[36] W. Sun, Z. Jiang, C. Xia, B. Hao, Y. Li, S. Yan, M. Wang, H. Liu, J. Ding, J. Liu, Z. Liu, J. Liu, H. Chen, D. Shen, and Y. Nie, Electronic structure of superconducting infinite-layer lanthanum nickelates, arXiv:2403.07344.

[37] X. Ding, Y. Fan, X. X. Wang, C. H. Li, Z. T. An, J. H. Ye, S. L. Tang, M. Y. N. Lei, X. T. Sun, N. Guo, Z. H. Chen, S. Sangphet, Y. L. Wang, H. C. Xu, R. Peng, and D. L. Feng, Cuprate-like electronic structures in infinite-layer nickelates with 3D dispersion, arXiv:2403.07448.

[38] L. Si, E. Jacob, W. Wu, A. Hausoel, J. Krsnik, P. Worm, S. Di Cataldo, O. Janson, and K. Held, Closing in on possible scenarios for infinite-layer nickelates: Comparison of dynamical mean-field theory with angular-resolved photoemission spectroscopy, Phys. Rev. Res. **6**, 043104 (2024).

[39] H. Lu, M. Rossi, A. Nag, M. Osada, D. F. Li, K. Lee, B. Y. Wang, M. Garcia-Fernandez, S. Agrestini, Z. X. Shen, E. M. Been, B. Moritz, T. P. Devereaux, J. Zaanen, H. Y. Hwang, K.-J. Zhou, and W. S. Lee, Magnetic excitations in infinite-layer nickelates, Science **373**, 213 (2021).

[40] P. Worm, Q. Wang, M. Kitatani, I. Biało, Q. Gao, X. Ren, J. Choi, D. Csontosová, K.-J. Zhou, X. Zhou, Z. Zhu, L. Si, J. Chang, J. M. Tomczak, and K. Held, Spin fluctuations sufficient to mediate superconductivity in nickelates, Phys. Rev. B **109**, 235126 (2024).

[41] P. Worm, L. Si, M. Kitatani, R. Arita, J. M. Tomczak, and K. Held, Correlations tune the electronic structure of pentalayer nickelates into the superconducting regime, Phys. Rev. Mater. **6**, L091801 (2022).

[42] H. LaBollita, M.-C. Jung, and A. S. Botana, Many-body electronic structure of $d^{9-\delta}$ layered nickelates, Phys. Rev. B **106**, 115132 (2022).

[43] Supplemental Information available at [URL will be inserted by publisher].

[44] S. Di Cataldo, P. Worm, J. Tomczak, L. Si, and K. Held, Unconventional superconductivity without doping in infinite-layer nickelates under pressure, Nature Comm. **15**, 3952 (2024).

[45] A. Georges, G. Kotliar, W. Krauth, and M. J. Rozenberg, Dynamical mean-field theory of strongly correlated fermion systems and the limit of infinite dimensions, Rev. Mod. Phys. **68**, 13 (1996).

[46] K. Held, Electronic structure calculations using dynamical mean field theory, Adv. Phys. **56**, 829 (2007).

[47] A. Toschi, A. A. Katanin, and K. Held, Dynamical vertex approximation: A step beyond dynamical mean-field theory, Phys Rev B **75**, 45118 (2007).

[48] A. A. Katanin, A. Toschi, and K. Held, Comparing pertinent effects of antiferromagnetic fluctuations in the two- and three-dimensional Hubbard model, Phys. Rev. B **80**, 75104 (2009).

[49] G. Rohringer, H. Hafermann, A. Toschi, A. A. Katanin, A. E. Antipov, M. I. Katsnelson, A. I. Lichtenstein, A. N. Rubtsov, and K. Held, Diagrammatic routes to nonlocal correlations beyond dynamical mean field theory, Rev. Mod. Phys. **90**, 25003 (2018).

[50] M. Kitatani, R. Arita, T. Schäfer, and K. Held, Strongly correlated superconductivity with long-range spatial fluctuations, Journal of Physics: Materials **5**, 034005 (2022).

[51] G. Kresse and J. Furthmüller, Efficient iterative schemes for ab initio total-energy calculations using a plane-wave basis set, Phys. Rev. B **54**, 11169 (1996).

[52] G. Kresse and J. Furthmüller, From ultrasoft pseudopotentials to the projector augmented-wave method, Phys. Rev. B **59**, 1758 (1999).

[53] J. P. Perdew, K. Burke, and M. Ernzerhof, Generalized gradient approximation made simple, Phys. Rev. Lett. **77**, 3865 (1996).

[54] J. P. Perdew, A. Ruzsinszky, G. I. Csonka, O. A. Vydrov, G. E. Scuseria, L. A. Constantin, X. Zhou, and K. Burke, Restoring the density-gradient expansion for exchange in solids and surfaces, Phys. Rev. Lett. **100**, 136406 (2008).

[55] A. A. Mostofi, J. R. Yates, Y.-S. Lee, I. Souza, D. Vanderbilt, and N. Marzari, wannier90: A tool for obtaining maximally-localised Wannier functions, Comput. Phys. Commun. **178**, 685 (2008).

[56] M. Wallerberger, A. Hausoel, P. Gunacker, A. Kowalski, N. Parragh, F. Goth, K. Held, and G. Sangiovanni, w2dynamics: Local one- and two-particle quantities from dynamical mean field theory, Comp. Phys. Comm. **235**, 388 (2019).

[57] M. Kitatani, T. Schäfer, H. Aoki, and K. Held, Why the critical temperature of high-T_c cuprate superconductors is so low: The importance of the dynamical vertex structure, Phys. Rev. B **99**, 41115 (2019).

[58] M. Kitatani, L. Si, P. Worm, J. M. Tomczak, R. Arita, and K. Held, Optimizing superconductivity: From cuprates via nickelates to palladates, Phys. Rev. Lett. **130**, 166002 (2023).

[59] P. Worm, Ph.D. thesis, TU Wien (2023).

[60] G. Kresse and J. Furthmüller, Efficient iterative schemes for *ab-initio* total-energy calculations using a plane-wave basis set, Phys. Rev. B **54**, 11169 (1996).

Supplemental Material:
Superconducting phase diagram of finite-layer nickelates $Nd_{n+1}Ni_nO_{2n+2}$

Andreas Hausoel ⬤, Simone Di Cataldo ⬤, Motoharu Kitatani ⬤, Oleg Janson ⬤, Karsten Held ⬤

(Dated: February 18, 2025)

In Supplemental Note SV, we present some details on the structural relaxation for the finite-layer nickleates and quantify the deviation from a planar Ni-O-Ni angle in the NiO_2 layers. In Supplemental Note SVI, details of the Wannier projection and the tight-binding parameters for the single Ni $d_{x^2-y^2}$ orbital are given. In Supplemental Note SVII and Supplemental Note SVII the density functional theory (DFT) and dynamical mean-field theory (DMFT) results of the main text is supplemented by the same figures for the other numbers of layers n considered. In Supplemental Note SIX we calculate the number of electrons in the DMFT A pockets.

SV.   CRYSTAL STRUCTURES

A.   Details on structural relaxation

The ground-state structures of $Nd_{n+1}Ni_nO_{2n+2}$ for the various number of layers $n = 2 - 7$ and ∞ is obtained using the conventional cell. Here, the in-plane lattice parameter is constrained to the one for the NGO substrate, i.e. $a = b = 3.83$Å. Then, the out-of-plane lattice parameter (c) is varied in a range of ±5Å around an initial guessed value of $\frac{\sqrt{3}}{2}(n+1)$, where n is the number of layers. For each value of c, the atomic positions is relaxed while the cell is kept fixed. The resulting curve of enthalpy vs c value is then fitted with a fourth-degree polynomial to determine the minimum, which was considered the relaxed value for the c axis. The values of c obtained in this way are then employed to construct the primitive cell. We note that the trend of c axis against n is perfectly linear, with $c = (6.56 \cdot n + 5.80)$Å

n	c (Å)
2	18.9
3	25.5
4	32.1
5	38.7
6	45.2
7	51.7

TABLE I. c axis values as a function of n obtained from the DFT relaxation.

There is considerable Ni-O-Ni out-of-plane distortion, visible with the naked eye in Fig. 1 (top) of the main text. In Fig. S6 we here additionally report the actual angle of this distortion for $n = 2 \ldots 7$. There is a large distortion at the stacking fault (the first and last layer), while the central layers are almost planar.
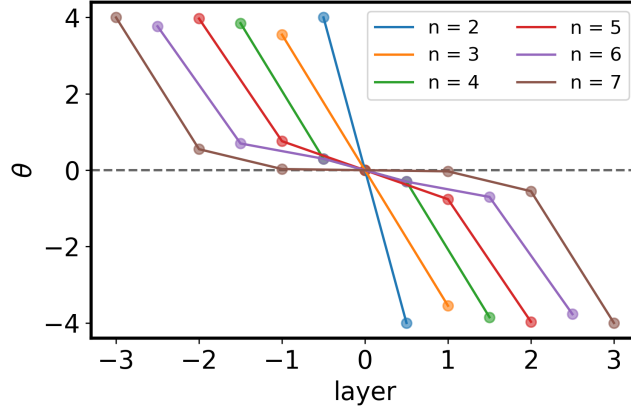
FIG. S6. Angle formed by the Ni–O bond with respect to the xy plane as a function of the layer number for finite-layer nickelates with $n = 2 - 7$ layers in total. The x axis indicates the layer number, with zero corresponding to the innermost layer.

SVI. WANNIER PROJECTION AND TIGHT-BINDING PARAMETERS

Maximally localized Wannier functions are obtained from the DFT band structure calculated using VASP [60] following the Marzari-Vanderbilt procedure as implemented in Wannier90 [55]. The non-self-consistent calculation of the Kohn-Sham eigenvalues is performed over an $8 \times 8 \times 8$ grid, with an energy cutoff of 1000 eV on the plane waves expansion. The disentanglement of the Wannierization is carried out with the energy windows specified in Tab. II, with a convergence tolerance of 10^{-10}Å^2 or up to 4200 iterations, with a mix ratio of 0.200. Minimization of the spread is carried out for 1200 iterations. In all cases we find that the spread of the Wannier functions is never larger than 3.0 Å^2. In Table II, we report in detail the outer energy window, the frozen energy window, and the initial projections, for each of the n layers.

number of layers	dis_win_min	dis_win_max	froz_win_min	froz_win_max	begin_projections
Ni d + Nd d; $10 \times n$-bands wannierization					
n = 2	-4.50	10.80	-1.19	2.61	Ni:d, Nd:d
n = 3	-4.87	10.13	-1.66	2.14	Ni:d, Nd:d
n = 4	-4.40	9.20	-1.89	1.71	Ni:d, Nd:d
n = 5	-6.18	9.72	-1.87	1.53	Ni:d, Nd:d
n = 6	-4.73	10.57	-2.22	0.58	Ni:d, Nd:d
n = 7	-3.77	10.53	-1.26	1.54	Ni:d, Nd:d
Ni - $d_{x^2-y^2}$; $1 \times n$-bands wannierization					
n = 2	-1.13	2.97	-0.13	0.37	Ni:$d_{x^2-y^2}$
n = 3	-1.40	2.73	-	-	Ni:$d_{x^2-y^2}$
n = 4	-1.63	2.67	-	-	Ni:$d_{x^2-y^2}$
n = 5	-1.37	2.92	-	-	Ni:$d_{x^2-y^2}$
n = 6	-1.32	2.58	-	-	Ni:$d_{x^2-y^2}$
n = 7	-2.49	4.01	-	-	Ni:$d_{x^2-y^2}$

TABLE II. Summary of the main Wannierization parameters for the various number of layers n. **Note:** to avoid machine or pseudopotential dependency, all the energy values are given with respect to the Fermi energy.

In Tables III to VIII we report the hopping parameters for the Wannier projection onto a single Ni $d_{x^2-y^2}$ orbital for the $Nd_{n+1}Ni_nO_{2n+2}$ series, with n going from 2 to 7. Here, t is the nearest neighbor hopping, t' the diagonal next-nearest neighbor hopping , t'' the next-next-neighbor hopping with two-site distance along the x (or y) direction, and t_z nearest neighbor hopping in the z-direction between the NiO$_2$ planes.

n = 2	t (eV)	t' (eV)	t'' (eV)	t'/t	t''/t	t_z (eV)
	-0.41	0.10	-0.06	-0.24	0.14	-0.06
	-0.41	0.10	-0.06	-0.24	0.14	

TABLE III. Hopping parameters for $n = 2$. The hoppings are listed in the order of the layers (from top to bottom). The interlayer hopping t_z between Ni-d$_{x^2-y^2}$ orbitals in adjacent layers is shown between one layer and the next.

n = 3	t (eV)	t' (eV)	t'' (eV)	t'/t	t''/t	t_z (eV)
	-0.42	0.10	-0.05	-0.24	0.12	-0.03
	-0.42	0.10	-0.05	-0.25	0.12	-0.03
	-0.42	0.10	-0.05	-0.24	0.12	

TABLE IV. As in Table IV but for $n = 3$.

n = 4	t (eV)	t' (eV)	t'' (eV)	t'/t	t''/t	t_z (eV)
	-0.41	0.10	-0.05	-0.24	0.13	-0.03
	-0.42	0.10	-0.05	-0.25	0.13	-0.03
	-0.42	0.10	-0.05	-0.25	0.13	-0.03
	-0.41	0.10	-0.05	-0.24	0.13	

TABLE V. As in Table IV but for $n = 4$.

n = 5	t (eV)	t' (eV)	t'' (eV)	t'/t	t''/t	t_z (eV)
	-0.41	0.10	-0.05	-0.24	0.13	-0.03
	-0.41	0.10	-0.05	-0.25	0.12	-0.03
	-0.41	0.11	-0.05	-0.25	0.12	-0.03
	-0.41	0.10	-0.05	-0.25	0.12	-0.03
	-0.41	0.10	-0.05	-0.24	0.13	

TABLE VI. As in Table IV but for $n = 5$.

n = 6	t (eV)	t' (eV)	t'' (eV)	t'/t	t''/t	t_z (eV)
	-0.41	0.10	-0.05	-0.25	0.13	-0.03
	-0.42	0.10	-0.05	-0.24	0.13	-0.03
	-0.41	0.10	-0.05	-0.25	0.13	-0.03
	-0.41	0.10	-0.05	-0.25	0.13	-0.03
	-0.42	0.10	-0.05	-0.24	0.13	-0.03
	-0.41	0.10	-0.05	-0.25	0.13	

TABLE VII. As in Table IV but for $n = 6$.

n = 7	t (eV)	t' (eV)	t'' (eV)	t'/t	t''/t	t_z (eV)
	-0.41	0.10	-0.05	-0.24	0.12	-0.02
	-0.41	0.10	-0.05	-0.24	0.12	-0.03
	-0.41	0.10	-0.05	-0.25	0.12	-0.03
	-0.41	0.10	-0.05	-0.25	0.12	-0.03
	-0.41	0.10	-0.05	-0.25	0.12	-0.03
	-0.41	0.10	-0.05	-0.24	0.12	-0.02
	-0.41	0.10	-0.05	-0.24	0.12	

TABLE VIII. As in Table IV but for $n = 7$.

SVII.   ADDITIONAL DFT RESULTS

In this Supplemental Note, we present in Fig. S7 the DFT band-structure and density of states (DOS) also for $n = 2$, $n = 3$, $n = 5$ and $n = 6$. The DFT results for $n = 4$ and $n = 7$, already presented in Fig. 2 of the main text, are repeated for convenience.
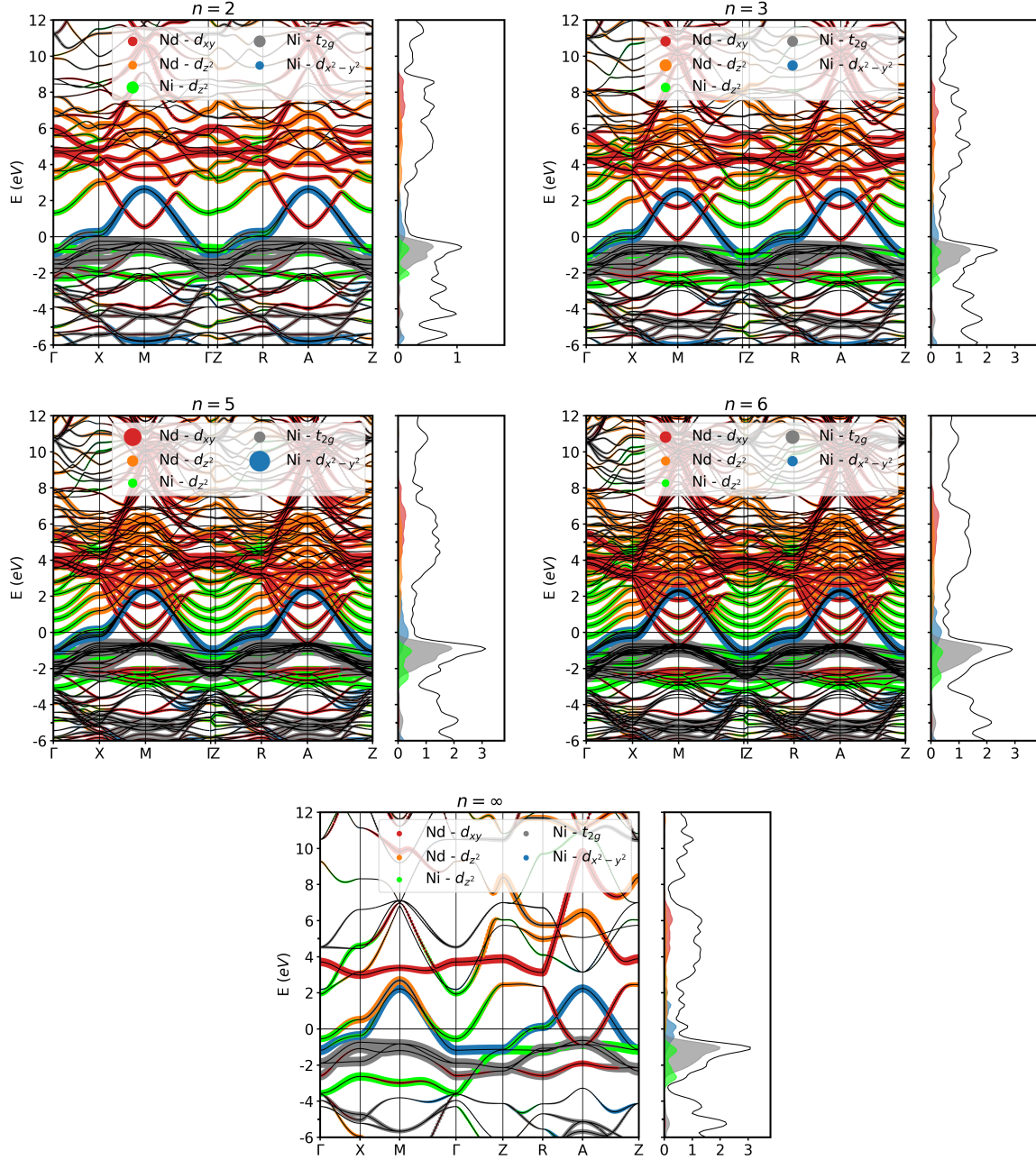

FIG. S7. DFT band structure for finite-layer nickelates $Nd_{n+1}Ni_nO_{2n+2}$ ($n = 2, 3, 5, 6, \infty$). The Fermi energy is taken as the energy zero. Projections onto different atomic orbitals are shown as thick colored lines, where thickness indicates the strength of the projection.

Further, in Fig. S8 we show the DFT Fermi surface for the finite-layer nickelates considered with $n = 2 \ldots 7$ layers, as well as for the infinite-layer nickelates. With the stacking fault well separating each n layers from the next n, there is essentially no k_z dispersion any more. Instead, we get n copies of the Ni $d_{x^2-y^2}$ and $n+1$ copies of the Nd d_{xy} orbital which forms the pocket around the A pocket momentum (see the $k_z = \pi$ plane) for the infinite-layer nickelate.
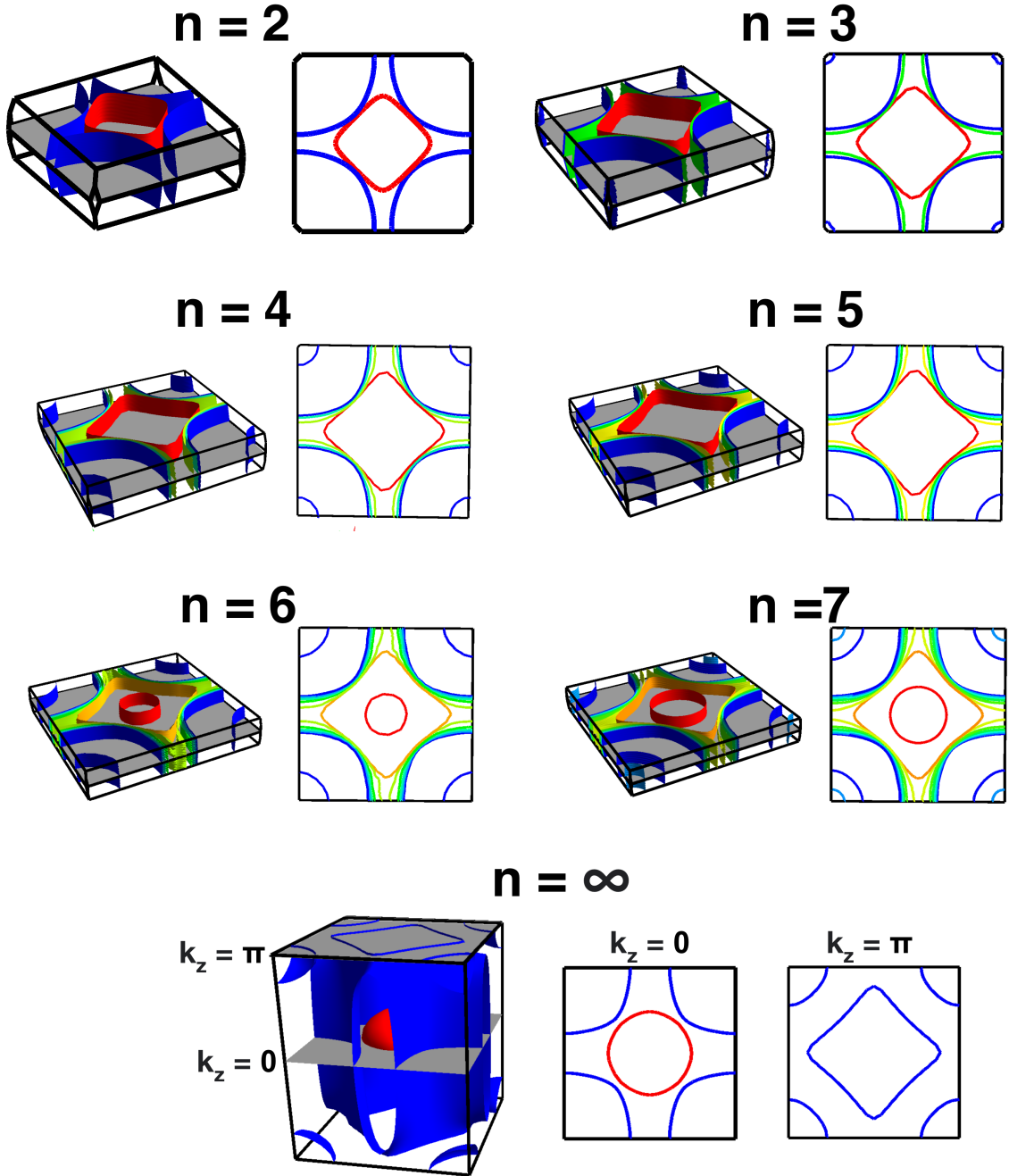
n = 2

n = 3

n = 4

n = 5

n = 6

n =7

n = ∞

$k_z = \pi$

$k_z = 0$

$k_z = 0$

$k_z = \pi$

FIG. S8. DFT-calculated Fermi surfaces for different number of layers n.

For the finite-layer nickelates, this pocket just emerges for $n = 2$ as a tube instead of a pocket, comprising the A and M point. For $n = 7$ a second tube emerges.

As for the Ni $d_{x^2-y^2}$ Fermi surface, we have for the infinite-layer case in Fig. S8, a hole-like Fermi surface for $k_z = 0$ and an electron-like for $k_z = \pi$. Concomitantly, we have both hole-like and electron-like Fermi surfaces for finite n, with the second electron-like Fermi surface appearing for $n = 5$.
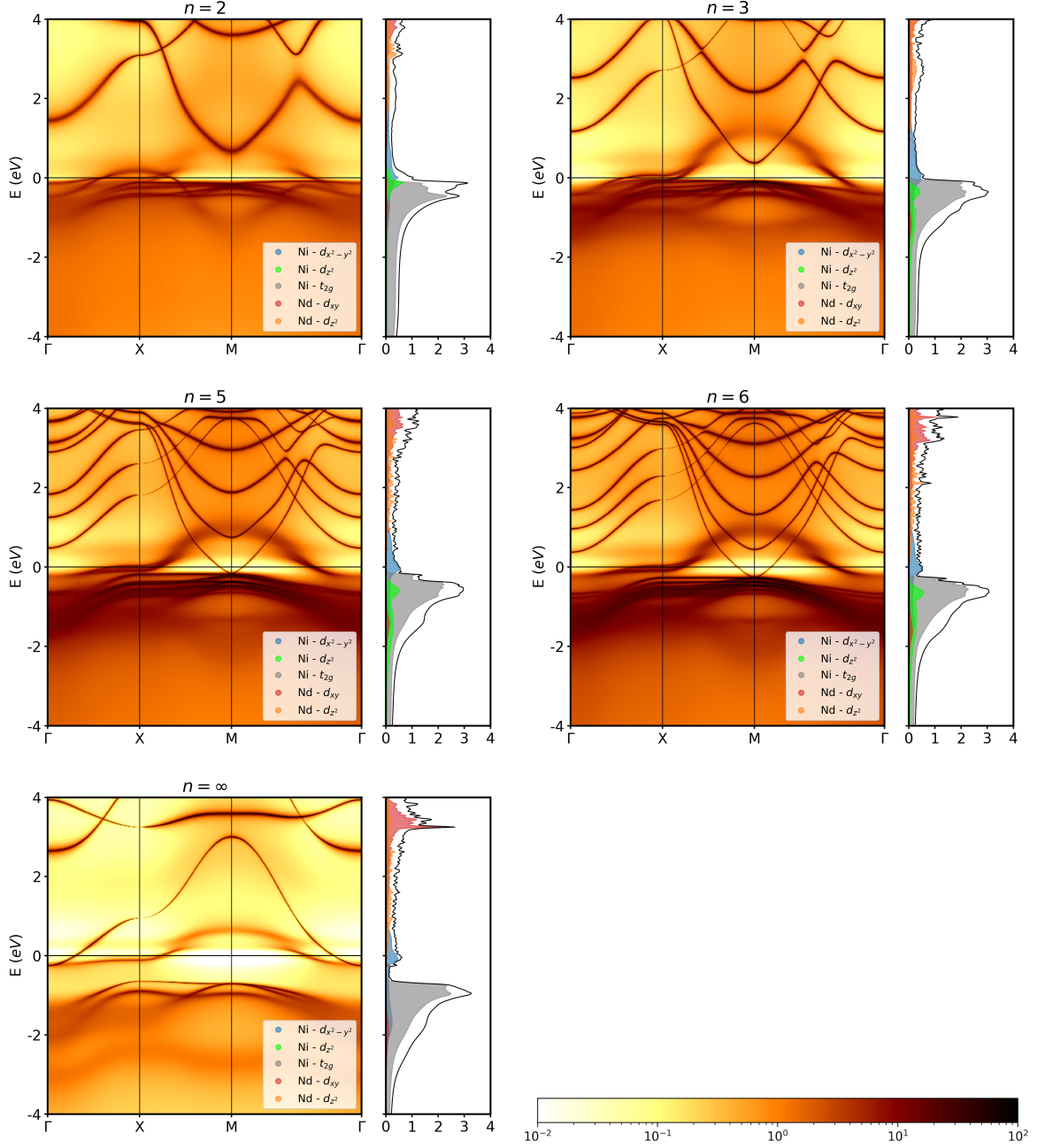
FIG. S9.   DMFT electronic structure and DOS of $Nd_{n+1}Ni_nO_{2n+2}$ for $n = 2, 3, 5, 6, \infty$ at room temperature.

SVIII.   ADDITIONAL DMFT RESULTS

In Fig. S9 we show, additionally to Fig. 3 of the main text, also the DMFT spectral function and DOS for $n = 2, 3, 5, 6$. For $n = 2$, the hole doping is so large that the DMFT physics turns: the Ni d_{z^2} orbital also crosses the Fermi level and we have actual multi-Ni-orbital physics. For $n > 2$ the qualitative behavior is similar, with as a matter of course more vineyard-like bands for larger n. Further we provide in Fig. S10 all calculated quasiparticle renormalizations.

In Fig. S11 we show the occupation for all atoms (layers) and all orbitals also for other n besides the $n = 7$ in Fig. 5 of the main text. Besides the DMFT results, also those of DFT, more precisely the DFT-derived Wannier Hamiltonian are shown. We notice for all n a somewhat larger DMFT occupation for the $d_{x^2-y^2}$ orbital than in DFT, but the tendency to have more holes in the layers interfacing the stacking fault is the same in DFT and DMFT. For
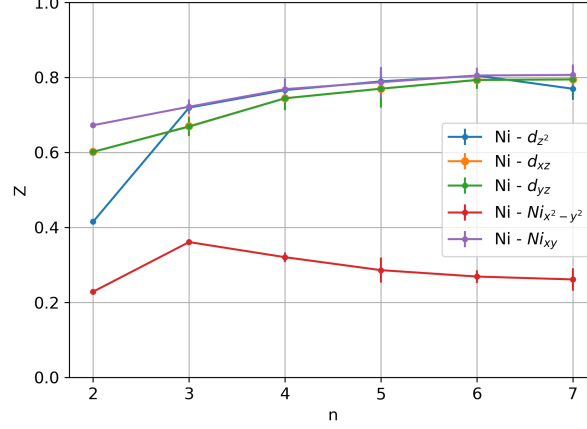
FIG. S10. Quasiparticle renormalizations of the Ni orbitals in DMFT as a function of the number of layers n at room temperature. Here, orbital 1 to 5 are the Ni z^2, xz, yz, $x^2 - y^2$ and xy orbital, respectively. The error bar reflects the variation of Z from layer to layer.

$n = 2$ the difference between DMFT and DFT occupation is strongly enhanced, as the DMFT Ni d_{z^2} orbital crosses the Fermi level.

While for $n = 3 \ldots \infty$ no orbital other than the predominantly Ni $d_{x^2-y^2}$ quasiparticle band and the Nd-d_{xy}-derived pocket cross the Fermi level, this orbital has some (albeit small) admixture with the Ni and Nd other orbitals. This admixture explains the deviations from the occupation $(1 - 1/n - \delta_{\mathrm{pocket}})/2$ of the Ni $d_{x^2-y^2}$ band, with δ_{pocket} determined in Supplemental Note SIX.

For example, in Fig. 2 of the main text or in Fig. S7 one sees that there is also a small Ni d_{z^2} contribution (green) to the predominantly Ni $d_{x^2-y^2}$ orbital at and below the X and R point. Vice versa there is a small Ni $d_{x^2-y^2}$ admixing to the other Ni bands below the Fermi energy (blue). Furhter, we observe a Ni t_{2g} admixture (grey) to the Nd d_{xy} band around A, and a somewhat larger admixture between Ni d_{z^2} and Nd d_{z^2} (green and orange).

For the orbital- and layer-resolved occupations in Fig. S11, this orbital admixture altogether leads to a Ni d_{z^2} occupation of 0.9 instead of 1, Ni $d_{xz/yz}$ of 0.97; Nd d_{z^2} of about 0.05 and Nd d_{xy} of about 0.15 (which is beyond what to expect from the A pocket size). For the nearly half-occupied Ni $d_{x^2-y^2}$ orbital these effects essentially cancel for $n > 4$ in DMFT. In contrast, the DFT occupations in Fig. 4 of the main text lie below $(1 - 1/n - \delta_{\mathrm{pocket}})/2$. In this respect, keep in mind though that the DFT pocket is larger than the plotted δ_{pocket} of DMFT and is already present for $n = 3$. The cancellation of the admixture effects in DMFT, is no longer valid for $n \lesssim 3$. The first reason for this is that there is essentially no hybridization with the outermost Nd orbitals: in Fig. S11 all Nd orbitals of the first and last layer are unoccupied, only those in the middle have a finite occupation because of the hybridization. For $n = 2$ a second major factor for the deviation from this analytical expectation is that the DMFT Ni d_{z^2} orbital now also crosses the Fermi level. It is thus much more depopulated, the Ni $d_{x^2-y^2}$ orbital vice versa closer to half-filling.
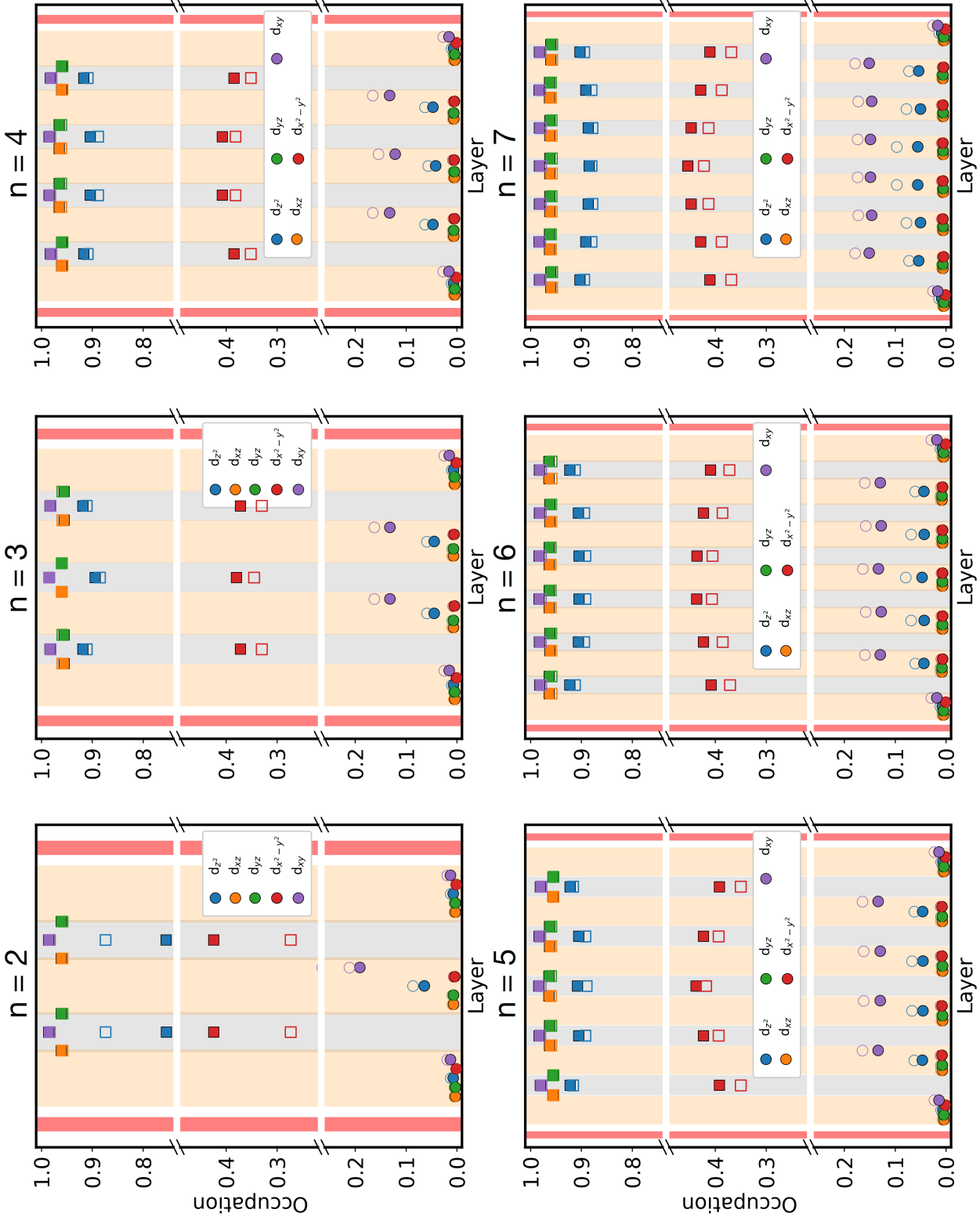
FIG. S11. Orbital- and layer-resolved Ni and Nd occupations for all the finite-layer compounds studied. The colored orange/grey/red stripes in the background represent the Nd, Ni, and defect O planes. Orbitals relative to Ni and Nd are represented respectively with squares and circles, while filled/hollow symbols indicate the DMFT and DFT (non-interacting Wannier Hamiltonian) result.

SIX.   ELECTRONS IN THE *A* POCKET

In Fig. S12 we show the calculated number of electrons in the A pocket as a function of the number of layers n. The extrapolated fit (black dashed line) is (rouned to 2 digits) $\delta_{\text{pocket}} = 0.02 - 0.08 \times 1/n$. The calculation of δ_{pocket} in DMFT is actually quite involved and outlined in the following. In short, we estimate the number of electrons by the volume of a cylinder representing the Fermi surface of the A–M pocket that also in DMFT is akin to the DFT Fermi surface in Fig. S8 (just shifted).
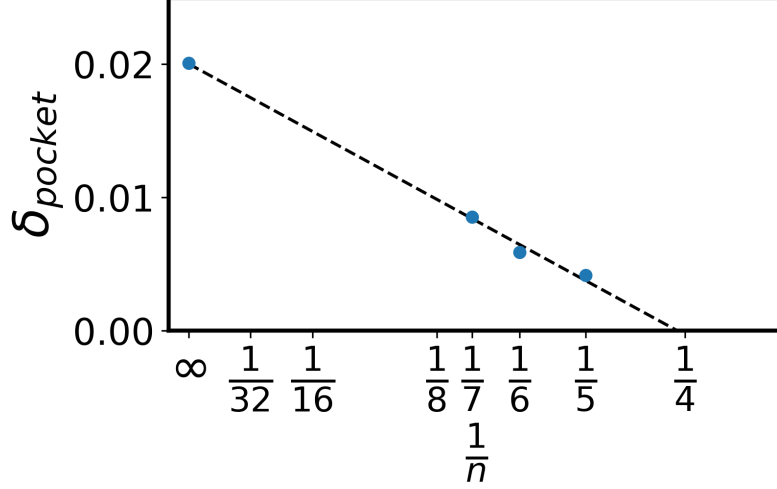

FIG. S12. Number of electrons in the *A* pocket as a function of the number of layers, normalized by the number of Ni atoms in the primitive cells. The black line indicates an extrapolated fit.

A.   Analytic calculation

To estimate the occupation of the pocket in the *A* point, we proceeded as follows. First, we observe (as shown in Fig. S8) that at the DFT level the Fermi surface forming *A* pocket is a cylinder with its axis going from *A* to *M*, and this is particularly true for $n \geq 5$. For the infinite-layer case, the pocket is instead rather spherical.

Considering that the number of states per unit volume in the reciprocal space is constant, and that each band contains up to two electrons (counting spin), the number of occupied states in a pocket can be calculated as

$$e_p^- = 2\frac{V_p}{V_{BZ}} \tag{S1}$$

Where V_p is the volume of the pocket, and V_{BZ} is the volume of the Brillouin zone.

a.   ***Ellipsoidal Fermi surface***   For a Fermi surface in the shape of an ellipsoid (quasi-spherical), the volume enclosed is

$$V_{p,s} = \frac{4}{3}\pi k_{Fx}k_{Fy}k_{Fz} \; , \tag{S2}$$

where k_{Fx}, k_{Fy}, k_{Fz} are the semi-axes of the spheroid, i.e. a sort of Fermi momentum, generalized to an ellipsoid. Substituting into Eq. (S1) we obtain that the number of states is

$$e_{p,s}^- = \frac{k_F^3 L_x L_y L_z}{3\pi^2} \; , \tag{S3}$$

where $L_x L_y L_z = V$ is the volume of the unit cell in real space.

b. ***Cylindrical Fermi surface*** For a cylindrical Fermi surface in a quasi-2D system, the volume enclosed is

$$V_{p,c} = \pi k_F^2 \frac{2\pi}{h} \tag{S4}$$

Where $\frac{2\pi}{h}$ is the height of the Brillouin zone in the shortest direction. Here k_F is to be intended as the radius of the cylinder, i.e. the Fermi momentum for the 2D case. Substituting into Eq. (S1) we obtain that the number of electrons in the A–M spheroid is

$$e_{p,c}^- = \frac{k_F^2 L_x L_y}{2\pi} \; , \tag{S5}$$

where $L_x L_y = A$ is the area of the top/bottom face of the unit cell in real space.

The $\mathbf{k_F}$ momentum can be identified as the $\mathbf{k}$ value for which the electron dispersion around the A pocket crosses the Fermi energy. This process must take into account the fact that electronic correlations tend to shift the pockets upwards in DMFT. To identify the momentum with the highest possible precision, we adopt the following process:

1. Superimpose the DMFT spectral function $A(\mathbf{k}, \omega)$ with the DFT bands, to find an energy shift ϵ^* such that the DFT band of the pocket corresponds to the maximum of the spectral function $A(\mathbf{k_F}, \omega = 0)$ (along the R–A line). An example for the case of $n = 5$ is shown in Fig. S13.

2. Calculate the DFT bands on an extremely dense array of points between R and A

3. Shift the DFT bands by ϵ^*, and find the momentum $\mathbf{k_F}$ for which they cross the Fermi energy.

4. As A is the center of the pocket, the vector $\Delta \mathbf{k} = \mathbf{k_F} - \mathbf{A}$ has modulus equal to the radius of the cylinder (or the ellipsoid semiaxis in the R–A direction)

5. **Spheroid only:** Repeat from point 2 along the A–M direction to obtain the size of the different semiaxis in that direction.

Note: due to the crystal symmetry, the radius of the cylinder must be the same in the x and y direction.
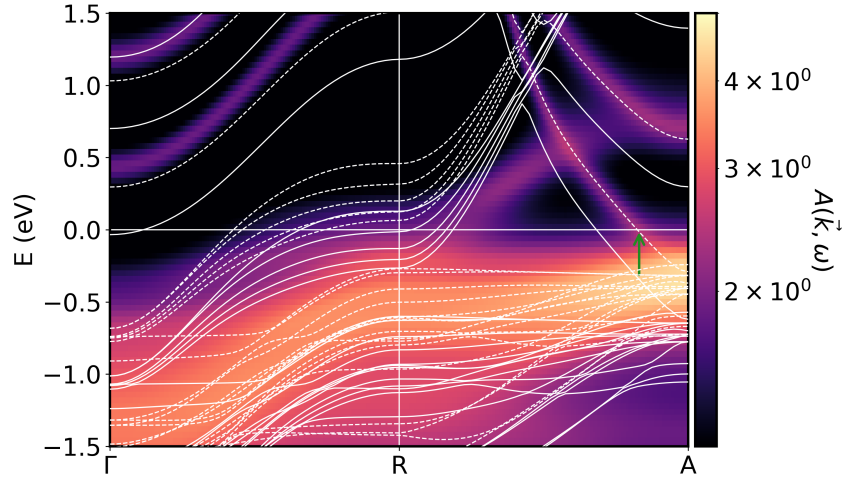

FIG. S13. Spectral function $A(\mathbf{k}, \omega)$ for $n = 5$ with DFT bands superimposed. The spectral function is indicated by the colormap, while unshifted DFT bands are shown as solid white lines, and shifted DFT bands as dashed white lines. The green arrow indicates the point in which the spectral function crosses the Fermi energy, which was used as reference to find the energy shift.